

Design and application of a confocal microscope for spectrally resolved anisotropy imaging

Alessandro Esposito,^{1,2,*} Arjen N. Bader,³ Simon C. Schlachter,²
Dave J. van den Heuvel,³ Gabriele S. Kaminski Schierle,² Ashok R. Venkitaraman,¹
Clemens F. Kaminski,^{2,4} and Hans C. Gerritsen³

¹The Medical Research Council Cancer Cell Unit, Hutchison/MRC Research Centre,
Hills Road, Cambridge CB2 0XZ, UK

²Department of Chemical Engineering and Biotechnology, University of Cambridge,
Pembroke St, Cambridge, CB2 1RA, UK

³Debye Institute, Utrecht University, PO Box 80.000, NL 3508 TA, Utrecht, The Netherlands

⁴SAOT School of Advanced Optical Technologies,
Friedrich Alexander University of Erlangen-Nuremberg, D-91058 Erlangen, Germany

*aesposito@quantitative-microscopy.org

Abstract: Biophysical imaging tools exploit several properties of fluorescence to map cellular biochemistry. However, the engineering of a cost-effective and user-friendly detection system for sensing the diverse properties of fluorescence is a difficult challenge. Here, we present a novel architecture for a spectrograph that permits integrated characterization of excitation, emission and fluorescence anisotropy spectra in a quantitative and efficient manner. This sensing platform achieves excellent versatility of use at comparatively low costs. We demonstrate the novel optical design with example images of plant cells and of mammalian cells expressing fluorescent proteins undergoing energy transfer.

©2011 Optical Society of America

OCIS codes: (110.4234) Multispectral and hyperspectral imaging; (170.3880) Medical and biological imaging; (180.1790) Confocal microscopy.

References and links

1. R. A. Neher, M. Mitkovski, F. Kirchhoff, E. Neher, F. J. Theis, and A. Zeug, "Blind source separation techniques for the decomposition of multiply labeled fluorescence images," *Biophys. J.* **96**(9), 3791–3800 (2009).
2. J. A. Palero, H. S. de Bruijn, A. van der Ploeg-van den Heuvel, H. J. C. M. Sterenborg, and H. C. Gerritsen, "In vivo nonlinear spectral imaging in mouse skin," *Opt. Express* **14**(10), 4395–4402 (2006).
3. P. L. T. M. Frederix, M. A. H. Asselbergs, W. G. J. H. van Sark, D. J. van den Heuvel, W. Hamelink, E. L. de Beer, and H. C. Gerritsen, "High sensitivity spectrograph for use in fluorescence microscopy," *Appl. Spectrosc.* **55**(8), 1005–1012 (2001).
4. T. S. Forde, and Q. S. Hanley, "Spectrally resolved frequency domain analysis of multi-fluorophore systems undergoing energy transfer," *Appl. Spectrosc.* **60**(12), 1442–1452 (2006).
5. A. Esposito, M. Gralle, M. A. C. Dani, D. Lange, and F. S. Wouters, "pHlameleons: a family of FRET-based protein sensors for quantitative pH imaging," *Biochemistry* **47**(49), 13115–13126 (2008).
6. A. Esposito, T. Tiffert, J. M. Mauritz, S. Schlachter, L. H. Bannister, C. F. Kaminski, and V. L. Lew, "FRET imaging of hemoglobin concentration in Plasmodium falciparum-infected red cells," *PLoS ONE* **3**(11), e3780 (2008).
7. A. N. Bader, E. G. Hofman, P. M. van Bergen En Henegouwen, and H. C. Gerritsen, "Imaging of protein cluster sizes by means of confocal time-gated fluorescence anisotropy microscopy," *Opt. Express* **15**(11), 6934–6945 (2007).
8. G. J. Kremers, E. B. van Munster, J. Goedhart, and T. W. Gadella, Jr., "Quantitative lifetime unmixing of multiexponentially decaying fluorophores using single-frequency fluorescence lifetime imaging microscopy," *Biophys. J.* **95**(1), 378–389 (2008).
9. S. Schlachter, S. Schwedler, A. Esposito, G. S. Kaminski Schierle, G. D. Moggridge, and C. F. Kaminski, "A method to unmix multiple fluorophores in microscopy images with minimal a priori information," *Opt. Express* **17**(25), 22747–22760 (2009).
10. D. S. Lidke, P. Nagy, B. G. Barisas, R. Heintzmann, J. N. Post, K. A. Lidke, A. H. Clayton, D. J. Arndt-Jovin, and T. M. Jovin, "Imaging molecular interactions in cells by dynamic and static fluorescence anisotropy (rFLIM and emFRET)," *Biochem. Soc. Trans.* **31**(5), 1020–1027 (2003).

11. K. A. Lidke, B. Rieger, D. S. Lidke, and T. M. Jovin, "The role of photon statistics in fluorescence anisotropy imaging," *IEEE Trans. Image Process.* **14**(9), 1237–1245 (2005).
12. A. H. A. Clayton, Q. S. Hanley, D. J. Arndt-Jovin, V. Subramaniam, and T. M. Jovin, "Dynamic fluorescence anisotropy imaging microscopy in the frequency domain (rFLIM)," *Biophys. J.* **83**(3), 1631–1649 (2002).
13. D. A. Bachovchin, S. J. Brown, H. Rosen, and B. F. Cravatt, "Identification of selective inhibitors of uncharacterized enzymes by high-throughput screening with fluorescent activity-based probes," *Nat. Biotechnol.* **27**(4), 387–394 (2009).
14. D. R. Matthews, L. M. Carlin, E. Ofo, P. R. Barber, B. Vojnovic, M. Irving, T. Ng, and S. M. Ameer-Beg, "Time-lapse FRET microscopy using fluorescence anisotropy," *J. Microsc.* **237**(1), 51–62 (2010).
15. F. T. S. Chan, C. F. Kaminski, and G. S. Kaminski Schierle, "HomoFRET fluorescence anisotropy imaging as a tool to study molecular self-assembly in live cells," *ChemPhysChem* (2011), doi:10.1002/cphc.201000833.
16. B. Valeur, and G. Weber, "Resolution of the fluorescence excitation spectrum of indole into the 1La and 1Lb excitation bands," *Photochem. Photobiol.* **25**(5), 441–444 (1977).
17. P. Blandin, S. Lévêque-Fort, S. Lécart, J. C. Cossec, M.-C. Potier, Z. Lenkei, F. Druon, and P. Georges, "Time-gated total internal reflection fluorescence microscopy with a supercontinuum excitation source," *Appl. Opt.* **48**(3), 553–559 (2009).
18. J. H. Frank, A. D. Elder, J. Swartling, A. R. Venkitaraman, A. D. Jeyasekharan, and C. F. Kaminski, "A white light confocal microscope for spectrally resolved multidimensional imaging," *J. Microsc.* **227**(3), 203–215 (2007).
19. J. Y. Ye, C. J. Divin, J. R. Baker, and T. B. Norris, "Whole spectrum fluorescence detection with ultrafast white light excitation," *Opt. Express* **15**(16), 10439–10445 (2007).
20. C. Dunsby, P. M. P. Lanigan, J. McGinty, D. S. Elson, J. Requejo-Isidro, I. Munro, N. Galletly, F. McCann, B. Treanor, B. Önfelt, D. M. Davis, M. A. A. Neil, and P. M. W. French, "An electronically tunable ultrafast laser source applied to fluorescence imaging and fluorescence lifetime imaging microscopy," *J. Phys. D Appl. Phys.* **37**(23), 3296–3303 (2004).
21. G. McConnell, "Confocal laser scanning fluorescence microscopy with a visible continuum source," *Opt. Express* **12**(13), 2844–2850 (2004).
22. M. A. Digman, V. R. Caiolfa, M. Zamai, and E. Gratton, "The phasor approach to fluorescence lifetime imaging analysis," *Biophys. J.* **94**(2), L14–L16 (2008).
23. Q. S. Hanley, and A. H. Clayton, "AB-plot assisted determination of fluorophore mixtures in a fluorescence lifetime microscope using spectra or quenchers," *J. Microsc.* **218**(1), 62–67 (2005).
24. S. Schlachter, A. D. Elder, A. Esposito, G. S. Kaminski, J. H. Frank, L. K. van Geest, and C. F. Kaminski, "mhFLIM: resolution of heterogeneous fluorescence decays in widefield lifetime microscopy," *Opt. Express* **17**(3), 1557–1570 (2009).
25. M. A. Rizzo, and D. W. Piston, "High-contrast imaging of fluorescent protein FRET by fluorescence polarization microscopy," *Biophys. J.* **88**(2), L14–L16 (2005).
26. T. J. van Ham, A. Esposito, J. R. Kumita, S. T. D. Hsu, G. S. Kaminski Schierle, C. F. Kaminski, C. M. Dobson, E. A. A. Nollen, and C. W. Bertoncini, "Towards multiparametric fluorescent imaging of amyloid formation: studies of a YFP model of alpha-synuclein aggregation," *J. Mol. Biol.* **395**(3), 627–642 (2010).
27. H. B. Manning, G. T. Kennedy, D. M. Owen, D. M. Grant, A. I. Magee, M. A. Neil, Y. Itoh, C. Dunsby, and P. M. French, "A compact, multidimensional spectrofluorometer exploiting supercontinuum generation," *J. Biophoton.* **1**(6), 494 (2008).
28. H. C. Gerritsen, A. V. Agronskaia, A. N. Bader, and A. Esposito, "Time Domain FLIM: theory, Instrumentation and data analysis," in *FRET & FLIM Imaging Techniques*, T. W. Gadella, ed. (Elsevier, Amsterdam, The Netherlands, 2009).
29. A. Esposito, H. C. Gerritsen, T. Oggier, F. Lustenberger, and F. S. Wouters, "Innovating lifetime microscopy: a compact and simple tool for life sciences, screening, and diagnostics," *J. Biomed. Opt.* **11**(3), 034016 (2006).
30. L. Pancheri and D. Stoppa, "A SPAD-based Pixel Linear Array for High-Speed Time-Gated Fluorescence Lifetime Imaging," 2009 Proc. of Esscirc, 429–432 (2009).
31. D. M. Grant, W. Zhang, E. J. McGhee, T. D. Bunney, C. B. Talbot, S. Kumar, I. Munro, C. Dunsby, M. A. Neil, M. Katan, and P. M. French, "Multiplexed FRET to image multiple signaling events in live cells," *Biophys. J.* **95**(10), L69–L71 (2008).
32. A. D. Jeyasekharan, N. Ayoub, R. Mahen, J. Ries, A. Esposito, E. Rajendra, H. Hattori, R. P. Kulkarni, and A. R. Venkitaraman, "DNA damage regulates the mobility of Brca2 within the nucleoplasm of living cells," *Proc. Natl. Acad. Sci. U.S.A.* **107**(50), 21937–21942 (2010).

1. Introduction

Biophysical tools are in high demand by the biomedical community for the study of molecular mechanisms underlying cell physiology, disease or diagnostics. For many applications, the possibility to quantify fluorescence emitted by several different fluorophores is often beneficial or necessary. Spectral imaging is very useful in this regard because it permits the simultaneous detection of a number of fluorophores through detection of their characteristic emission spectra [1–4]. Furthermore, many fluorophores exhibit altered emission spectra as a

function of the molecular environment thus allowing quantitative sensing applications [5]. Also fluorescence anisotropy and fluorescence lifetime have been used for sensing applications [6,7] and, less frequently, for unmixing [8,9]. The development of a sensor for the combined detection of fluorescence emission and excitation spectra, anisotropy and lifetime would enable multiplexed sensing capabilities that could be exploited for biological assays. This provided the motivation for the design and characterization of the spectropolarimeter for confocal laser scanning microscopy presented here to establish a first step towards such imaging modality.

Fluorescence anisotropy imaging microscopy relies on the excitation of the sample by polarized light causing the preferential excitation of fluorophores that are orientated along the electric field vector of the excitation light. The degree of polarization of the fluorescence emission can be then measured by detecting fluorescence intensities along the same orientation ($I_{//}$) or along the orthogonal direction (I_{\perp}) with respect to the excitation light. The fluorescence anisotropy is then defined as $r = (I_{//} - G I_{\perp}) / (I_{//} + 2G I_{\perp})$ where G is a correction factor that accounts for different transmission efficiencies of the system for the two polarization components in the signal [10,11]. Small organic fluorophores, free or conjugated with small biomolecules (e.g., short peptides or DNA oligos), rotate very fast compared to their fluorescence lifetime, with the latter typically in the 1-10 ns range, resulting in significant depolarization of fluorescence emission ($r \rightarrow 0$). When such small molecules bind to larger interacting partners, they rotate more slowly and tend to preserve the characteristic limiting anisotropy [12] of the fluorophores (typically $r \rightarrow 0.3-0.4$). This method is at the basis of common *in vitro* assays for high throughput screening in drug discovery programs [13]. The capability to measure fluorescence anisotropy over different spectral bands simultaneously increases information content and throughput of such techniques even further. Larger fluorophores, for instance fluorescent proteins or small organic fluorophores, which are covalently bound to large molecules, rotate slowly compared to their fluorescence lifetime. Therefore, the high fluorescence anisotropy of such fluorophores ($r \rightarrow 0.3-0.4$) will thus typically not be increased by binding events. On the contrary, the opposite may be observed: energy migration phenomena (e.g., Förster resonance energy transfer or FRET) [14,15] lead to loss of polarisation and hence an decrease of anisotropy. This occurs because multiple energy transfer steps between randomly oriented molecules lead to successive loss of polarisation. Here again, the potential to measure anisotropy in a number of spectral channels is highly beneficial permitting for example the discrimination of several FRET reporters simultaneously greatly expanding on current capabilities of conventional fluorescence anisotropy microscopes. Polarisation resolved excitation spectra have furthermore great use in the characterization of electronic states of fluorophores [16]. Coupling an instrument capable of detecting emission anisotropy spectra with a tunable excitation source, for example a supercontinuum source [17–21] would offer the unique capability of mapping out full emission-excitation spectral matrices for both polarization components in the signal thus offering a complete characterization of the probed fluorophore state in biological samples. In this paper we describe the development of a confocal laser scanning spectropolarimeter and its application in two novel ways. First, we demonstrate how the spectropolarimeter can be used to gain contrast in bioimaging that cannot otherwise be obtained. The very large information content acquired is challenging to represent and we illustrate new methods for the visualization of corresponding information. Secondly, we show a novel method with potential to image FRET in biological samples by measuring fluorescence emission spectra.

Engineering a spectropolarimeter for bioimaging applications poses two major challenges. Firstly, the detection system has to be very efficient in order to minimize photon losses which would hinder its application to the detection of the low fluorescence signals that are typical in biological applications. Secondly, the read-out of the spectral information has to be fast enough to be synchronized with the scanners of a confocal microscope to enable acquisition speeds that are compatible with the study of biological samples. These challenges have to be

balanced against the requirement for a cost-effective system that is simple to use and maintain; critical points to ensure the widespread use by the biomedical community. Therefore, we engineered a simple yet powerful instrument for the simultaneous and orthogonal dispersion of different colors and polarization states of fluorescence onto a single two-dimensional electron-multiplying charge coupled detector (EMCCD).

In order to resolve some ambiguity of terms like “multi-dimensional imaging”, “multi-parametric imaging” and “hyper-spectral imaging”, we propose to refer to this class of imaging modalities as hyper-dimensional imaging microscopy (HDIM). HDIM refers explicitly to the additional dimensionality that spectroscopic properties of the sample add to an image. Here, we present the engineering of a hyper-dimensional imaging microscope based on a unique spectropolarimeter and its demonstration on a plant sample, *Convallaria majalis*, and on mammalian cells expressing linked fluorescent proteins undergoing FRET.

2. System engineering

A compact spectropolarimeter (Fig. 1A) was developed with the use of a Wollaston prism (MWQ25-05-HEAR450-750nm, by Karl Lambrecht Corp., USA) that introduces a 0.5 degrees angular dispersion between the two orthogonal polarization components which are then relayed to a MgF₂ coated 25mm SF11 glass equilateral prism (Edmund Optics Ltd., UK) positioned at the minimum deviation angle (~61 degrees). The orthogonal angular dispersions introduced by the two prisms were then transformed in linear displacement by either a 3 cm or 4 cm achromatic anti-reflection coated doublet for Fig. 1–5, respectively. Spectropolarimetry was implemented on two commercial confocal microscopes: a Nikon C1 (Nikon Instruments Europe BV, The Netherlands) and an Olympus FV300 (Olympus Medical, United Kingdom). The light source was directly coupled to the scan-head to achieve control of the polarization of the excitation light. Both microscopes were upgraded with “slow-scan boards” provided by the manufacturers to permit a pixel dwell-time in the order of 120-200 μ s. The performance of the two systems was comparable; the images shown here were acquired with the FV300 coupled to a supercontinuum source (SC400, Fianium, UK) and filtered by an acousto optical tunable filter (AOTF; AOTFnC-400.650 AA Electrooptics), as described in an earlier publication [18]. The fastest operation of the spectropolarimeter was achieved by slaving the confocal scanners to a master pixel clock signal generated by the on-board electronics of the EMCCD. The slightly divergent beam emerging from the confocal pinhole was reflected by a first mirror (M1) and collimated by an achromatic doublet (400 mm). The scanning lens (s) of the confocal and the collimating lens (L1) of the spectropolarimeter together with the scanners (xy), dichroic (d) and M1 constitute a beam expander designed to deploy a ~5mm beam to the prisms. M1 and M2 are silver coated mirrors used for the alignment of the spectropolarimeter. The two irises (I1-2) and mirrors (M1-2) were used iteratively to ensure that the beam entered the spectropolarimeter centered and parallel to its optical axis. For the coarse alignment of the system, excitation light reflected by a mirror positioned at the sample plane can be tracked at positions O1 and O2. All the optics and optomechanics were from Thorlabs Ltd. (UK) or machined in house unless otherwise indicated. This configuration permitted the fewest number of optical components to be used and thus minimized optical losses, whilst also allowing a comparatively simple alignment of the system.

Two commercial back illuminated EMCCDs were tested: a Cascade 128 + by Photometrics (USA) and an iXon860 by Andor Technology (UK). Both EMCCDs provided similar results during bench tests; however, the iXon860 was our final choice because of the comprehensive SDK for Matlab provided by Andor Technology that facilitated the development of Matlab (The MathWorks, USA) code. Matlab code was used for both real-time operation of the camera and processing of the data.

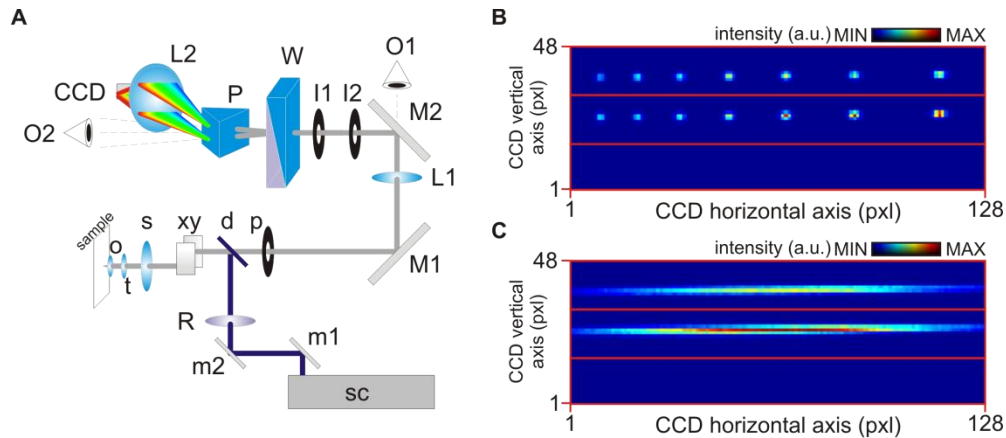


Fig. 1. (A) Schematic of principal components in spectropolarimeter; R: half-wave plate retarder; M1-2: silver coated alignment mirrors; L1: collimating lens; O1-2: alignment spots; I1-2: alignment apertures; W: Wollaston prism; P: equilateral dispersive prism; L2: camera lens sc: supercontinuum source and acousto-optical tuneable filter; m1-2: dielectric alignment mirrors; d: dichroic mirror or 80/20 beam splitter; xy: x-y scanners; s: scanning lens; o: objective; t: tube lens; p: confocal pinhole. (b) Typical laser comb used for the calibration of the system with the half-wave plate rotated at 22.5 degrees. (c) Typical spectrum of a fluorescent plastic slide detected on the sensor with the half-plate oriented at 0 degrees.

3. Calibration of the system

All fluorescence images shown here were acquired with a pixel dwell-time between 120 and 190 μ s, using a 60x oil-immersion objective and 256x256 pixels (~6s total acquisition time). 15-24 additional pixels were acquired during the retracing of the laser. These pixels were removed from the final images. The nominal resolution of the spectrograph was 2-5nm over the 470-700nm spectral range. The spectropolarimeter is aligned by setting the half-wave plate at 22.5 degrees relative to the (polarization) axis of the spectropolarimeter. Seven laser lines were selected by the AOTF [18], reflected from a glass coverslip and imaged on the EMCCD. Figure 1B shows the part of the EMCCD sensor (~50x128 pixels) used for imaging and calibration with wavelengths selected from 470 nm to 530 nm every 10 nm. The indicated regions serve for the alignment of the two prisms, the EMCCD and the spectral calibration of the device. Once the alignment and calibration are completed, the half-wave plate is reset to 0 degrees. Figure 1C shows the doubly dispersed fluorescence emitted by a fluorescent plastic slide (Chroma Technologies Corp., USA) with the half-wave plate at 0 degrees. The dependency of the deviation angle of the Wollaston prism on wavelength is evidently negligible; indeed, the Wollaston prism permits the projection of two parallel spectra onto a well defined area of the EMCCD sensor. For each pixel of the confocal image, three horizontal lines (Fig. 1C) of the sensors are read-out with vertical binning typically set at 15-20 pixels. Two strips gather the polarization dependent spectra; the third line is used for background subtraction. These areas are indicated by the red rectangles in Fig. 1B and 1C. Fluorescence from YFP expressed in mammalian cells (corresponding to $r = 0.3$) was used for the calibration of the anisotropy values. A flat field correction was applied to the spectra by normalizing each spectral bin to its relative (spectral) width.

4. Imaging spectropolarimetry

A hyper-dimensional data set provides a wealth of information that one cannot fully represent with two-dimensional maps. Therefore, to the engineering of new hardware dedicated to HDIM, it is necessary to develop novel strategies for the analysis and visualization of hyper-dimensional data sets. Figure 2 shows possible representations of the data acquired from the plant *Convallaria majalis* (Leica Microsystems Ltd., Milton Keynes, UK). Figure 2A shows

the average intensity of the sample obtained by summing the hyper-dimensional data stack along both spectral and polarization dimensions. This image is a map of fluorescence intensities that could be measured with a typical confocal microscope. The additional spectral information of the data set is visualized in Fig. 2B where the intensities measured over the spectral elements were summed over three spectral ranges (<495 nm, 495-570nm and >570 nm) to provide a true color image of the sample [2]. This was obtained summing the hyper-dimensional data set along the polarization dimension. On the other hand, summing along the spectral dimension allows mapping the anisotropy of the sample (Fig. 2C).

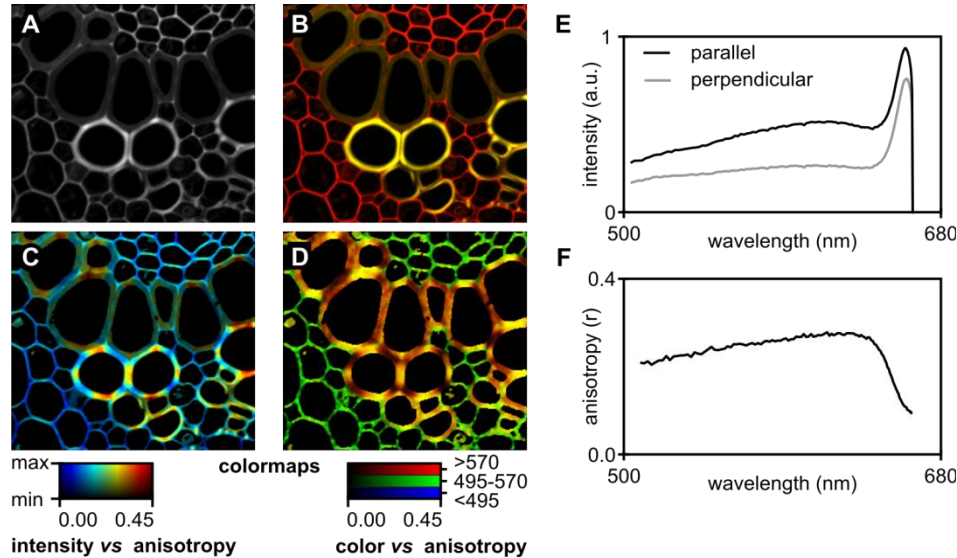


Fig. 2. Spectral and polarization resolved imaging of *Convallaria majalis* stained with Safranin and Fast Green fluorophores. Panel A shows the average intensity emitted over the entire spectral range upon excitation at 485 nm. B. True color representation of the sample. Panel C shows the anisotropy of the sample overlaid on the intensity map. The information shown in panels B and C is consolidated in panel D. Here, spectral information is contained in the RGB coloring and intensity represents the anisotropy. The bi-dimensional look-up-tables for panel C and D are shown at the bottom. Panels E and F show the spatially averaged emission and anisotropy spectra of the sample.

The brightness of Figs. 2A–2C is proportional to the intensity of the sample (see look-up table below panel C). By discarding the intensity information and remapping the anisotropy measured over the three spectral bands <495nm, 495-570nm and >570nm, it is possible to obtain a combined spectral/anisotropy image (Fig. 2D). The corresponding color – anisotropy look-up table is shown below panel D. The red- green- blue- (RGB) representations show the spectral information and the brightness of the image is proportional to the measured anisotropy values. Note when comparing Fig. 2B and Fig. 2D that areas first shown in red subsequently appear in green. This is caused by the low anisotropy values of the red emitter and the high anisotropy levels of the green fluorescence. This is evident from Fig. 2E and 2F where the spatially averaged emission spectra of the sample for both polarization states and the spatially averaged anisotropy spectrum are shown. It is clear that the combination of spectral and anisotropy information provides enhanced contrast.

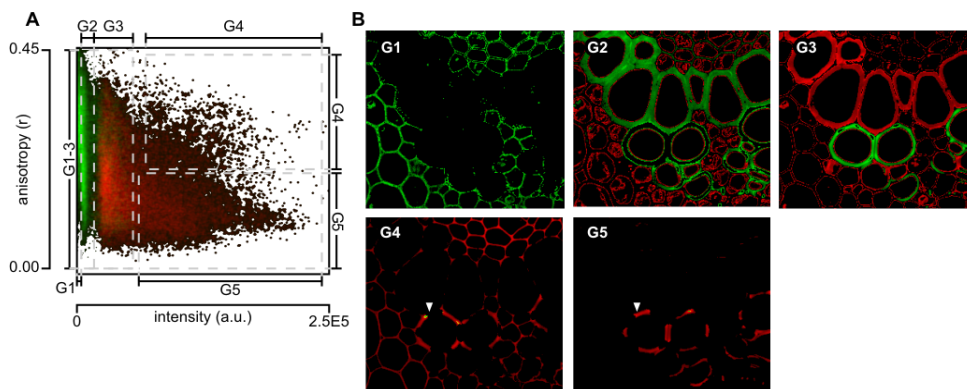


Fig. 3. Fluorograms permit the segmentation of HDIM data sets. The fluorescence anisotropy is plotted versus the intensities measured in the red (>570 nm) and green (495-570 nm) spectral regions (A). This fluorogram aided the segmentation of different structures by separating different “clouds” of pixels by gating intensities and anisotropy values (G1-5). The segmented images are shown in panel B; the white arrows show different structures (G4-5) that are segmented based on differences in their anisotropy.

A simultaneous visualization of the entire information content encoded in the hyper-dimensional images is impossible. Their interpretation can be simplified, however, by discarding the spatial information. This strategy has been used successfully in fluorescence lifetime imaging microscopy to provide a model-free method to segment images [22–24]. Figure 3 shows a bi-dimensional histogram (scatter plot) obtained by plotting fluorescence anisotropy values *versus* intensity for each pixel. Each point is again RGB color coded as in Fig. 2D. Spectral, anisotropy and intensity information are visualized simultaneously in this new type of RGB-fluorogram. Corresponding pixels in the images can be segmented by setting specific gates to select pixels that exhibit specific correlation between anisotropy and intensity. An example of such segmentation is given in Fig. 3. Regions G1-5 in the scatter plot (Fig. 3A) are selected and used to segment the original image resulting in the images in Fig. 3B. The white arrows in Fig. 3B (images labeled G4 and G5) show different structures that are segmented by anisotropy and that would be indistinguishable merely via their emission spectra. Differences in anisotropy values may be caused by energy migration events and by fluorophore orientation effects.

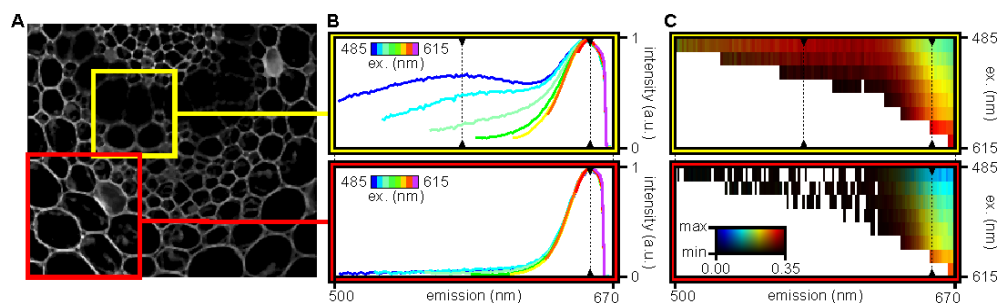


Fig. 4. Excitation and emission resolved anisotropy spectra. Two regions of interest (yellow and red) of the intensity image are selected (A) and emission spectra are shown as a function of excitation wavelength (B). C summarizes the entire spectral information acquired by the imaging spectropolarimeter in combination with the tuneable supercontinuum source.

HDIM provides enhanced contrast and segmentation of biological samples that can be further increased by including excitation spectra [9]. Excitation and emission resolved images can be acquired with the spectropolarimeter by using a supercontinuum excitation source in combination with an AOTF [18]. It was thus possible to fully characterize and map the steady-state fluorescence emission of a sample as shown in Fig. 4. For each excitation

wavelength in the range of 485-615 nm 8 hyper-dimensional images were acquired and averaged. Regions of interest (yellow and red squares in Fig. 4A) were selected and emission spectra were extracted for the different excitation wavelengths (Fig. 4B). The upper (yellow) region of interest clearly contains additional fluorescing components that emit in the blue-green spectral range that are only excited at short wavelengths.

Emission (abscissa), excitation (ordinate), anisotropy (color), intensity (brightness) matrices for the two regions of interest are shown in Fig. 4C. These matrices represent the full spectral signature of the sample and permit to appreciate the presence of a red fluorophore with a very large Stokes shift exhibiting low anisotropy (in both regions) and a green fluorophore with a small Stokes shift exhibiting high anisotropy values (in the upper region of interest).

5. FRET detection by imaging spectropolarimetry

Another potential application of imaging spectropolarimetry is for the detection of FRET, i.e. the non-radiative transfer of excitation energy from a donor fluorophore to an acceptor fluorophore [25]. FRET causes depolarization of the sensitized emission because of the transfer of excitation energy to a second fluorophore the orientation of which is not constrained by the photoselection rules of the directly excited fluorophores. A decrease in the anisotropy can be measured when identical fluorophores are in close proximity (homo-FRET) allowing protein oligomerization to be detected [7,26]. Recently, Rizzo and Piston [25] demonstrated that mapping the FRET-dependent depolarization in hetero-FRET experiments could be also useful to measure protein-protein interactions. Imaging spectropolarimetry can be applied to the imaging of FRET-based assays. Indeed, Fig. 5A shows the HeLa cells expressing a fusion construct of the Cyan Fluorescent Protein (CFP) and the Yellow Fluorescent Protein (YFP) separated by a 17 amino acid long linker. This construct exhibits a FRET efficiency of about 25% (determined by TCSPC in independent experiments). The same sample was either excited at 440 nm to excite CFP or at 490 nm to directly excite the acceptor YFP. Also a HeLa cell co-expressing non-linked variants of CFP and YFP (i.e. not exhibiting FRET) is shown in the bottom panels of Fig. 5A. Figure 5B shows spatially averaged anisotropy spectra if the samples shown in Fig. 5A. The no-FRET sample exhibits an average anisotropy in the CFP and YFP emission band of ~ 0.2 and ~ 0.3 , respectively. These values are molecular properties of the two fluorophores in the cellular environment. Also the CFP-17AA-YFP exhibits $r \sim 0.3$ for the YFP fluorophore directly excited at 490nm. Again, this is a molecular property of the directly excited YFP. Because of FRET, the same construct exhibits a remarkable depolarization (from 0.3 to 0.2) in the YFP emission when excited at 440nm. This depolarization is clearly present only in the emission of the acceptor fluorophore as shown from the ratio of the anisotropy spectra of the FRET samples to the no-FRET sample (Fig. 5B, bottom panel). Note that when the sample was excited at 490 nm, a 530-550 nm band pass filter was added in front of the spectropolarimeter; therefore, the anisotropy curve for this measurement (Fig. 5B, dark yellow) is shown only in the region where the acquired light intensity was sufficient to compute anisotropy values.

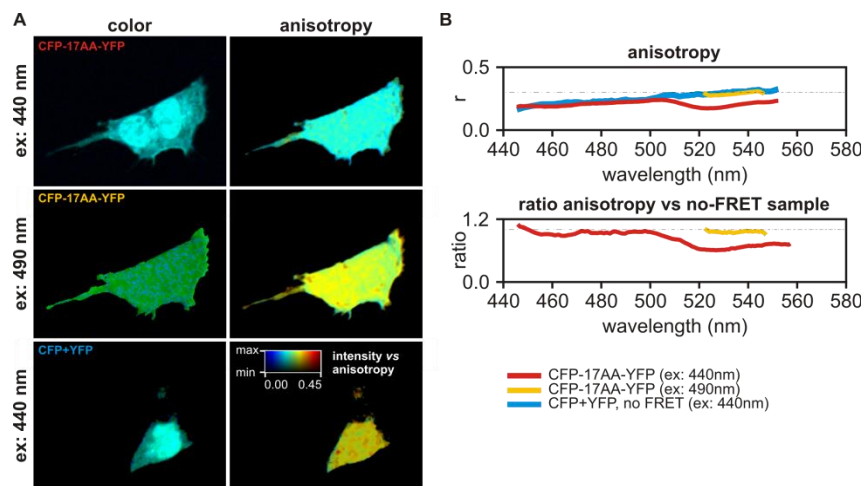


Fig. 5. Spectropolarimetry imaging of a FRET pair. (A) Color and anisotropy images of a cell expressing a CFP-17AA-YFP fusion construct (top two rows) are shown when either the donor or the acceptor fluorophores are excited at 440 nm or 490 nm, respectively. When the sample is excited at 490 nm, a 530-550 nm band pass filter was placed before the detector. Also, a cell expressing separated (non-linked) CFP and YFP is shown in the bottom row. Spatially averaged anisotropy spectra (B, top) of these images are shown in red (440 nm excitation) and dark yellow (490 nm excitation). The reference anisotropy spectrum is shown in cyan (no-FRET sample). The ratio between the anisotropy spectra of the samples exhibiting 25% FRET efficiency and the no-FRET sample (B, bottom) clearly show a depolarization caused by FRET present only in the acceptor emission.

6. Discussion

The many properties of fluorescence light can be detected with the use of traditional detectors. However, detection of spectra and polarization requires the use of many detectors [27] or the sequential acquisition of images using different filters or analyzers. Generally, these strategies would result in increase complexity and costs of the microscopy system or the detrimental loss of photons, respectively. Therefore, we developed and characterized an optimized confocal laser scanning spectropolarimeter for the simultaneous and photon-efficient measurement of fluorescence spectra and polarization. Care was taken to minimize optical losses and cost, while maximizing ease of use. The integration of the EMCCD camera into a confocal system is comparatively straightforward and it permits high sensitivity, high spectral resolution spectral imaging due to its high quantum efficiency (> 90%) and large number of pixels. These properties yield a system far superior to commercially available spectral imaging systems. As a first step to fully resolve all photophysical properties of a biological sample, we were able to simultaneously acquire fluorescence spectral and polarization information. Furthermore, with the use of a supercontinuum light source, the full spectral signature of the sample could be recorded. Importantly, a hyper-dimensional detector collects all the photons harvested by the confocal microscope. These photons are then histogrammed by the spectropolarimeter in the relevant spectral and polarization channels. No change of polarizer or filter was used in order to achieve high photon-efficiency and time resolution. The confocal spectropolarimeter operates at a maximum (hyper-dimensional) pixel rate of 8 kHz, thus providing a confocal image of 256x256 pixels in about 6 seconds. Images of 512 x 512 pixels can be acquired in ~30 seconds. This acquisition speed is significantly slower than that found commercial confocal laser scanning microscopes, but it should be noted that the information content of the images generated with the confocal spectropolarimeter is far higher (256 spectral/polarization channels). Furthermore, this acquisition speed is certainly compatible with many biological applications and it is much faster than other biophysical imaging modalities already broadly used [28].

This system can be further enhanced in two ways. Firstly, two-photon excitation with a Ti:Sapphire laser will improve the dynamic range for anisotropy imaging by an increase of the maximum anisotropy from 0.4 to 0.57. A tunable Ti:Sapphire will also allow two-photon excitation fingerprinting similar to what we demonstrated for one-photon excitation with the supercontinuum light source. Secondly, the EMCCD will be replaced by time-resolved detectors that will allow the measurement of individual photon arrival times. These technologies are already available and will enable extension to time-resolved spectropolarimetry [29,30].

The content rich images provided by HDIM and other new imaging techniques pose new challenges for data analysis and visualization. We proposed here types of representation to permit the intuitive visualization of data sets obtained by imaging spectropolarimetry. The most important applications that we foresee for hyper-dimensional imaging microscopy include (i) unmixing of multiple FRET-based biosensors [31], (ii) detection of interactions in multi-molecular complexes and (iii) enhanced contrast for tissue imaging. In our laboratories, HDIM will complement existing techniques that we are using for probing the molecular mechanisms underlying neurodegeneration [26] and cancer [32]. However, it is likely that HDIM will find numerous applications not only in biology and biophysics but also in material sciences and spectroscopy.

Acknowledgements

AE is funded by the EPSRC (grant EP/F044011). GSSK is supported by grants from EPSRC and the Wellcome Trust. CFK gratefully acknowledges funding from the BBSRC (BB/H023917/1), the EPSRC (EP/H018301/1), the MRC (G0902243), and the Wellcome Trust / MRC (089703/Z/09/Z). We would like to thank John Gannon, Wei-Yao Ma, Berrie Goddard, Jim Thompson (Cambridge University) for their contribution to the project and the mechanical workshop at Utrecht University. We would like to thank also Andor Technology, Photometrics and Nikon Europe for their assistance and for providing demo systems.